Acta Geotechnica
https://doi.org/10.1007/s11440-025-02683-y

RESEARCH PAPER

Benchmarking thermo-hydro-mechanical models for geological barrier integrity in clay-based repositories

Eric Simo[1,2] · Christophe de Lesquen[3] · Minh-ngoc Vu[3] · Simon Raude[4] · Ginger El Tabbal[4] · Asta Narkuniene[5] · Povilas Poskas[5] · Frédéric Collin[6] · Rawat Abhishek[6] · Hangbiao Song[6] · Antonio Gens[7] · Fei Song[7,11] · Rocio Paola Leon-Vargas[2] · Alexandru-Bogdan Tatomir[8] · Miguel Mánica[9] · Thomas Nagel[1,10,12] · Jörg Buchwald[1,10]

Received: 22 January 2025 / Accepted: 27 May 2025

Abstract
This study investigates the thermo-hydro-mechanical (THM) behavior of argillaceous formations, particularly the Callovo–Oxfordian (COx) claystone, over extended timescales to evaluate the long-term safety of radioactive waste repositories. Numerical simulations were performed as part of a benchmark exercise to study the response of the COx formation under heating scenarios representative of high-level radioactive waste disposal. Six modeling teams from various institutions participated in this benchmark, using various numerical codes, providing valuable information on the evolution of temperature, pore water pressure, and stresses within the repository environment, particularly around the disposal cells. The results highlight that the COx formation exhibits significant thermal pressurization and stress relaxation because of its low permeability, whereas the excavation damaged zone (EDZ) remains confined to the near field and does not extend significantly under the thermal load considered. The study demonstrates the robustness of numerical tools for repository safety assessments and emphasizes the importance of validated THM formulations to ensure long-term containment of radioactive waste.

Keywords Callovo–Oxfordian claystone · Deep geological disposal · High-level radioactive waste · Thermo-hydro-mechanical modeling

1 Introduction

Throughout Europe, argillaceous rocks are preferred as potential formations for the geological disposal of radioactive waste due to their inherent self-sealing characteristics, low permeability, limited molecular diffusion, and retention capacity for radionuclides [see, e.g., 17, 31]. The performance of a repository within these formations is significantly influenced by thermo-hydro-mechanical (THM) processes [22]. Therefore, a comprehensive understanding of the THM properties of these clayey materials is crucial for the effective design and safety assessment of repository systems.

Assessing the long-term safety of repository systems requires numerical models and tools capable of accurately simulating the observed THM behavior of the host rock and predicting the evolution of the repository over long timescales. Ensuring the accuracy and reliability of these predictive tools is essential, requiring a verification and validation procedure [29] that addresses process models, material knowledge, as well as the code and data base in an integrated manner [41].

As part of the HITEC project [11], a research work package within the European Joint Programme on Radioactive Waste Management (EURAD), various modeling teams from European countries were invited to participate in a benchmarking initiative aimed at evaluating the reliability of the numerical tools and the collective

Eric Simo, Christophe de Lesquen, Minh-ngoc Vu, Simon Raude, Ginger El Tabbal, Asta Narkuniene, Povilas Poskas, Frédéric Collin, Rawat Abhishek, Hangbiao Song, Antonio Gens, Fei Song, Rocio Paola Leon-Vargas, Alexandru-Bogdan Tatomir, Miguel Mánica, Thomas Nagel, and Jörg Buchwald have contributed equally to this work.

Extended author information available on the last page of the article

Published online: 18 July 2025

ability to accurately predict the THM evolution of radioactive waste repositories in various clay host formations. In a previous work [40], a theoretical case study was conducted aimed at verifying the THM formulations of different numerical codes, leading to satisfactory consistency. In this study, the selected benchmark exercise focuses on simulating the effect of increasing temperature on the integrity of a clay formation due to the disposal of heat-generating radioactive waste. Here, integrity refers to the preservation of the properties of barriers in the repository system, which are critical for the safe containment of waste.

In clay formations, previous studies suggest that the increase in temperature will induce a significant response of the rock [4, 16, 35, 38, 43]. Among the phenomena that can negatively affect the host rock, thermally induced pore water pressures and the reduction in clay strength due to increased temperature are the most significant response of the rock [4, 28, 42]. This work focuses on the potential risk associated with the first phenomenon. To achieve this, various modeling teams conducted coupled THM numerical simulations to analyze the evolution of a repository system within the Callovo–Oxfordian (COx) formation, utilizing different numerical codes. The results of these modeling endeavors are discussed in the present study.

2 Benchmark description

The proposed benchmark focuses on simulating the effects of heating in a radioactive waste repository within a clay formation. This study is motivated by the concept of disposal that is being considered in France by the French National Radioactive Waste Management Agency (ANDRA) [2]. This modeling exercise aims to provide detailed information on the response of the geological barrier to nuclear waste disposal, toward the objective of a safer and more effective repository design.

The simulation aims to analyze the THM behavior of a repository system in the COx argillite over a period of 1000 years. The COx is an indurated hard clay that forms part of the Jurassic formation of the Parisian Basin [15], and it is the host rock selected for the disposal facility to be built in France [18]. The numerical model includes a vertical column from the surface to a depth of 1000 m, with a specific focus on a horizontal disposal borehole located at a depth of 480 m. Figure 1 shows the stratigraphic column considered; details on the lithological description can be found elsewhere [33]. The borehole, with a diameter of 1 m, lies in the center of the model, which extends horizontally for 25 m, mirroring the distance between adjacent cells. Only two-dimensional (2D) analyses are performed, assuming plane strain deformation. Lateral boundaries act as lines of symmetry, thereby representing an infinite number of cells in the horizontal direction. This accounts for the influence of adjacent cells and seeks to represent the conditions found at the central area of an emplacement field for high-level waste (HLW) and spent fuel (SF)/HLW tunnels.

The initial temperature considers the natural geothermal gradient, assumed equal to $0.025\,\mathrm{K\,m^{-1}}$, starting from a surface temperature of 10°C. The in situ stress at each depth reflects the overburden, with specific horizontal stress conditions and an initial overpressure in the COx formation based on field observations [3, 44]. The minor horizontal total stress (σ_h) is assumed equal to the vertical total stress (σ_v). The major horizontal total stress (σ_H) is equal to σ_v in the Kimmeridgian and equal to $1.3\sigma_h$ from the top of the COx layer and downward, with the disposal boreholes being parallel to σ_H. A hydrostatic pore water pressure is assumed except at the COx, where an overpressure is considered. Figure 2 shows the water pressure and total stress profiles employed.

The thermal load under consideration is based on a COG-800 waste package. Specifically, each 100 m long borehole is intended for the disposal of 42 such packages. From the moment they are installed in the borehole, the thermal load will gradually decrease as shown in Fig. 3. For the purposes of this study, two distinct scenarios are considered. In the first scenario, the packages are introduced into the cell after a preliminary cooling period of 85 years, resulting in an initial thermal load of $139\,\mathrm{W\,m^{-1}}$. The second scenario assumes a shorter cooling duration of 55 years, resulting in a higher initial thermal load of $242\,\mathrm{W\,m^{-1}}$. This high-power case was chosen to induce fracturing and is not representative of a deep geological repository.

The sequential processes involved in waste disposal are represented by the boundary conditions applied to the excavation wall. The benchmark is divided into three phases, described below and summarized in Table 1:

- Excavation phase (1 day): the initial stresses at the borehole wall are linearly reduced to zero representing the immediate post-excavation state. The pore water pressure is also linearly reduced to atmospheric conditions. In this phase, no thermal load is applied.
- Waiting phase (2 years): stresses at the borehole wall are linearly increased from 0 to 3 MPa to represent the effect of swelling of the backfill in the annular space between the borehole and the lining. This phase spans over two years, and during this time, no water or heat flow occurs at the borehole wall.
- Heating phase (1000 years): no water flow is considered, and boundary stresses are maintained at a constant value of 3 MPa. However, during this phase heat flow is applied at the borehole wall according to the assumed

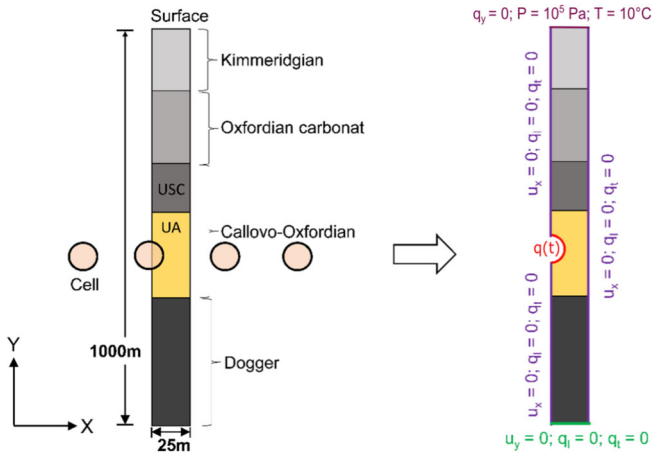

Fig. 1 Model geometry and boundary conditions for the far-field benchmark (USC and UA refer to the silto-carbonated and clayey subunits, respectively, of the COx formation) [11]

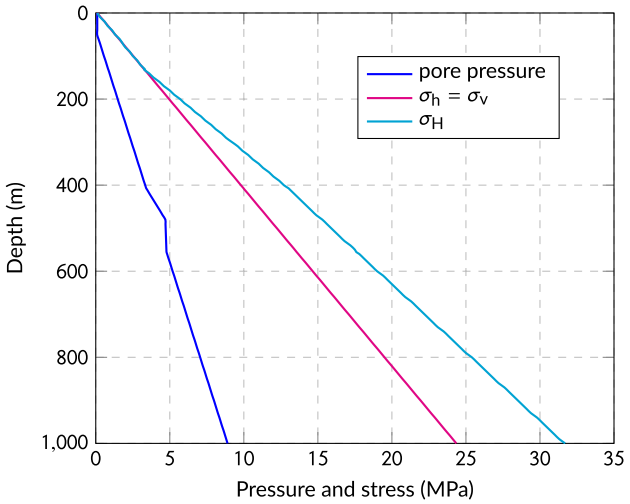

Fig. 2 Profiles of pore water pressure, vertical total stress (σ_V), and minor (σ_h) and major horizontal total stresses (σ_H) employed [11]

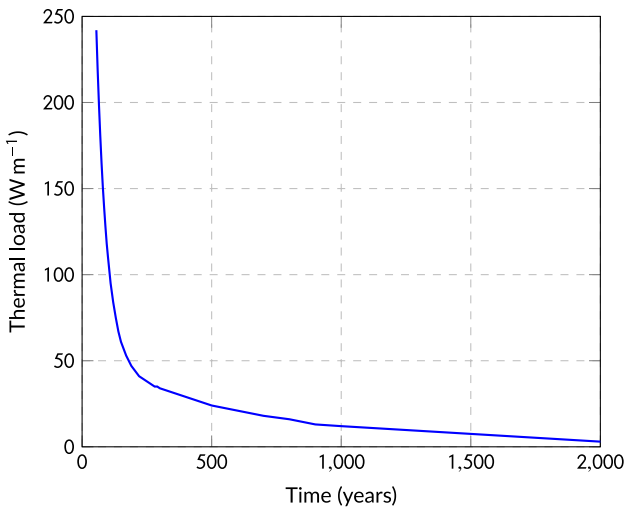

Fig. 3 Evolution of thermal load from a waste package [11]

evolution of the thermal load from the waste package (Fig. 3) and the corresponding cooling scenario (85 or 55 years).

The COx formation is divided into the silto-carbonated subunit (USC), the transition subunit (UT), and the clayey subunits UA1, UA2, and UA3, with UA2 and UA3 sharing the same parameters. Their thermo-poro-elastic and hydraulic properties are listed in Tables 2 and 3, whereas the properties of the remaining formation are summarized in Table 4. An isotropic linear elastic model was assumed for the Kimmeridgian, Oxfordian carbonate, Dogger, and the COx subunit USC. In contrast, a cross-anisotropic linear elastic model was employed for the COx subunits UT and UA. The physical properties of water and air are summarized in Table 5.

It is important to remark that typical model parameters—including permeability, porosity, elastic moduli, thermal conductivity, and Biot coefficients—are subject to inherent variability due to natural geological heterogeneity and measurement uncertainties. Sensitivity analyses conducted in similar studies (e.g., [32, 39]) show that parameters like Young's modulus, permeability, and thermal conductivity have significant effects on pore pressure evolution and temperature profiles. Small variations in permeability, particularly in low-permeability claystone formations, can markedly influence the magnitude and duration of thermal pressurization. The current benchmark study assumes fixed parameter sets based on experimental data from the literature compiled in [11], ensuring consistency among modeling teams.

In Tables 3 and 4, scalar Biot coefficients were assumed for all geological units. It is well known that the use of a scalar Biot coefficient is a simplification that does not fully reflect the anisotropic nature of poromechanical coupling in transversely isotropic materials such as the COx

Table 1 Boundary conditions at the borehole wall

Phase	Mechanical	Hydraulic	Thermal
Excavation (1 day)	Stress reduction to 0% of the initial in situ stress	Pore water pressure reduced linearly to p_{atm} (0.1MPa)	No flow
Waiting (2 years)	Linear stress increase from 0 to 3 MPa	No flow	No flow
Heating (1000 years)	Constant stress of 3 MPa	No flow	Thermal flow based on applied power prediction (Fig. 3)

Table 2 Thermo-poro-elastic and hydraulic properties of the COx formation (Part 1) [11]

Parameters	Units	Subunit	Value
Porosity, n	$--$	USC	0.15
		UT, UA	0.18
Bulk density, ρ	$kg\,m^{-3}$	USC	2480
		UT, UA	2386
Young's modulus normal to bedding, $E_\perp$	GPa	USC	12.8
		UT	8.5
		UA2-UA3	7
		UA1	10
Young's modulus parallel to bedding, $E_\parallel$	GPa	UA & UT	$1.5 \times E_\perp$
Isotropic Poisson's ratio, v	–	USC	0.3
Anisotropic Poisson's ratios	$--$	UT, UA	$v_{\parallel\parallel} = 0.2$
			$v_{\perp\parallel} = 0.3$
			$v_{\parallel\perp} = 0.45$

Table 3 Thermo-poro-elastic and hydraulic properties of the COx formation (Part 2) [11]

Parameters	Units	Subunit	Value
Shear modulus normal to bedding, $G_{\perp\parallel}$	GPa	UT	3.8
		UA2-UA3	3.1
		UA1	4.4
Linear thermal expansion coefficient, α_S	K^{-1}	USC, UT, UA	$1.28 \cdot 10^{-5}$
Thermal conductivity normal to bedding, $\lambda_\perp$	$W\,m^{-1}\,K^{-1}$	USC	1.8
		UT	1.4
		UA2-UA3	1.25
		UA1	1.6
Thermal conductivity parallel to bedding, $\lambda_\parallel$	$W\,m^{-1}\,K^{-1}$	USC	1.8
		UT, UA	$1.5 \times \lambda_\perp$
Specific heat, c_S	$J\ kg^{-1}\,K^{-1}$	USC, UT, UA	790
Intrinsic permeability parallel to bedding, $k_\parallel$	m^2	USC, UT, UA	$3.9 \cdot 10^{-20}$
Intrinsic permeability normal to bedding, $k_\perp$	m^2	USC, UT, UA	$1.3 \cdot 10^{-20}$
Biot coefficient, b	$--$	UA & UT, USC	0.8

claystone. While a tensorial Biot coefficient would be more appropriate for representing directional dependencies, this feature is not yet supported in all modeling codes used in the benchmark. For consistency and comparability, an

Table 4 Thermo-poro-elastic and hydraulic properties of the Kimmeridgian, Oxfordian carbonate, and Dogger formations [11]

Parameters	Units	Kimm.	Oxfordian	Dogger
Porosity, n	–	0.13	0.13	0.10
Bulk density, ρ	$\mathrm{kg\,m^{-3}}$	2450	2470	2470
Young's modulus, E	GPa	3.6	30	30
Poisson's ratio v	$--$	0.3	0.3	0.3
Linear therm. expansion coef., α_S	$\mathrm{K^{-1}}$	$2.2 \cdot 10^{-5}$	$4.5 \cdot 10^{-6}$	$4.5 \cdot 10^{-6}$
Therm. cond., λ	$\mathrm{W\,m^{-1}\,K^{-1}}$	$\lambda_\perp = 1.1 \quad \lambda_\parallel = 1.4\lambda_\perp$	2.3	2.3
Specific heat, c_S	$\mathrm{J\,kg^{-1}\,K^{-1}}$	1024	925	925
Int. permeability, k	$\mathrm{m^2}$	10^{-19}	10^{-16}	10^{-18}
Biot coefficient, b	–	0.6	0.75	0.6

Table 5 Water and air physical properties

Parameter: water (w) and air (a)	Units	Values
Density ρ_w	$\mathrm{kg\,m^{-3}}$	1000
Compressibility at 40°, β_w	$\mathrm{Pa^{-1}}$	$4.5 \cdot 10^{-10}$
Thermal conductivity, λ_w	$\mathrm{W\,m^{-1}\,K^{-1}}$	0.528
Specific heat, c_w	$\mathrm{J\,kg^{-1}\,K^{-1}}$	4180
Density, ρ_a	$\mathrm{kg\,m^{-3}}$	1.205
Dynamic viscosity, μ_a	Pa.s	$1.80 \cdot 10^{-5}$
Thermal conductivity, λ_a	W/m/K	0.025
Specific heat, c_a	J/kg/K	1000

isotropic Biot coefficient was therefore applied uniformly across all simulations. The implications of this simplification should be considered in future work as code capabilities evolve.

Finally, it is important to mention that assuming an elastic behavior for the host rock represents a significant simplification, since these indurated clayey materials exhibit other behavioral features such as plastic deformations, rate dependence, and creep, as well as a quasi-brittle response with significant softening after peak strength under low and moderate confining pressures [27]. As a result, these materials are particularly challenging from a modeling point of view. Nevertheless, the main objective of this work is to highlight the importance of THM coupling for integrity assessments of repositories in indurated clay formations, particularly in the far field, as well as to demonstrate the robustness of the numerical tools employed by leading research institutions in the field. Therefore, using an elastic constitutive description is considered reasonable.

However, an additional analysis is presented in Sect. 5, where a more detailed constitutive description [27] was adopted, including time-dependent deformations and the dependence of mechanical properties on temperature, to assess the effect of inelastic processes in the COx formation.

The coefficient of volumetric thermal expansion for water is assumed to vary with temperature, as described by the polynomial in Eq. 1 [24], with the resulting temperature variation shown in Fig. 4.

$$\alpha_w \times 10^{-4} = \left(4 \times 10^{-6}\right)T^3 - (0.001)T^2 + (0.1404)T - 0.3795 \quad (1)$$

where α_w is the coefficient of volumetric thermal expansion for water in $^\circ\mathrm{C}^{-1}$.

Similarly, the temperature dependence of water viscosity is also considered. The following relationship, put forward by [37], is assumed in this benchmark:

$$\mu = \mu_0\, e^{A+\frac{B}{C+T}} \quad (2)$$

where μ_0 is a coefficient with units of viscosity (mPa · s), $A = -3.719$ (unitless), $B = 578.919$ °C, $C = -137.546$ °C, and T is the temperature in °C. This relationship is displayed graphically in Fig. 4.

Six distinguished modeling teams from various European institutions participated in this benchmark exercise. The participants included ANDRA, Bundesgesellschaft für Endlagerung mbH (BGE), Électricité de France SA (EDF), the Lithuanian Energy Institute (LEI), the University of Liège (ULiege), and the Polytechnic University of Catalonia (UPC). The numerical codes employed by each team are presented in Table 6. The results are expected to be evaluated in terms of effective stresses, temperature, and pore water pressure at specific points around the borehole and at the far boundary, see Table 7.

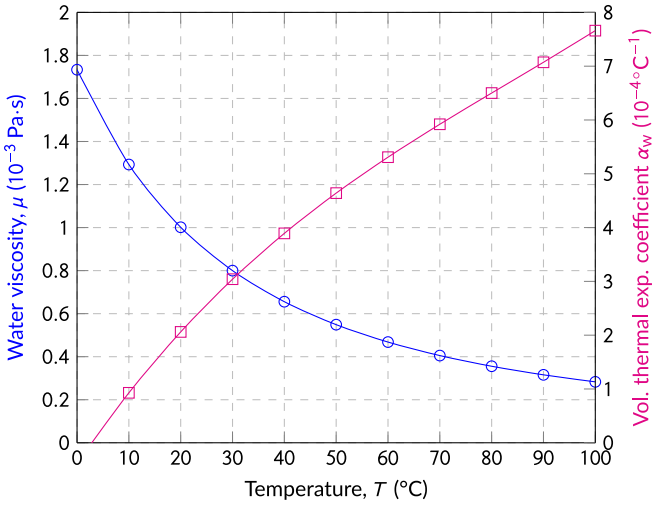

Fig. 4 Water viscosity and volumetric thermal expansion coefficient as functions of temperature

Table 6 Involved modeling teams and their respective codes

Organization	Country	Numerical code
ANDRA	France	COMSOL
BGE	Germany	OpenGeoSys
EDF	France	Code_Aster
LEI	Lithuania	COMSOL
ULiege	Belgium	LAGAMINE
UPC	Spain	Code_Bright

Table 7 Coordinates of observation points in meter

Points	Coordinates	Points	Coordinates
P1	(0.5, − 480.0)	P4	(5.0, − 480.0)
P2	(1.0, − 480.0)	P5	(10.0, − 480.0)
P3	(2.0, − 480.0)	P6	(25.0, − 480.0)

3 Numerical model

3.1 Governing equations

The THM formulations employed in the various computational codes are grounded in the theory of porous media. The medium under consideration is conceptualized as a volumetric mixture composed of a homogeneous solid matrix interspersed with pores. The prevailing assumption is that these pores are filled by two phases, typically a liquid and a gas phase. In the context of fully saturated media, only the liquid phase is accounted for. The classical model for such a saturated porous medium, as elaborated by [36], constitutes the foundation upon which the governing equations are constructed. Different versions have been systematically compared in [34]. The balance equations encompass the energy, mass, and momentum of the system, each described briefly below.

The energy balance is governed by an advection–diffusion equation that accounts for heat advected by fluid movement as well as conductive heat transfer through all phases:

$$\left(\rho C_p\right)^{\text{eff}}\frac{\partial T}{\partial t}+\rho_{\text{FR}}C_{p\text{F}}\nabla T\cdot\tilde{\mathbf{w}}_{\text{FS}}-\text{div}\left[\lambda^{\text{eff}}\nabla T\right]=Q_T \tag{3}$$

where $\left(\rho C_p\right)^{\text{eff}}$ is the effective volumetric heat capacity of the porous medium, ρ_{FR} is the density of the fluid phase, $C_{p\text{F}}$ is the specific heat capacity of the fluid, $\tilde{\mathbf{w}}_{\text{FS}}$ is the fluid filter velocity relative to the solid, λ^{eff} is the effective thermal conductivity of the porous medium, Q_T is the heat source term, and ∇T is the temperature gradient.

The water mass balance, incorporating fluid and solid compressibility and the poroelastic response of the matrix, is given by:

$$\left(\phi_{\text{F}}\beta_{p\text{F}}+\frac{\alpha_{\text{B}}-\phi_{\text{F}}}{K_{\text{SR}}}\right)\frac{\partial p}{\partial t}-\left(\phi_{\text{F}}\beta_{T\text{F}}+(1-\phi_{\text{F}})\boldsymbol{\alpha}_{T\text{S}}:\boldsymbol{I}\right)\frac{\partial T}{\partial t}+\alpha_{\text{B}}\text{div}\,\dot{\mathbf{u}}+\text{div}\,\tilde{\mathbf{w}}_{\text{FS}}=Q_H \tag{4}$$

where p is the fluid pressure (Pa), ϕ_{F} is the porosity, $\beta_{p\text{F}}$ is the fluid compressibility under pressure, α_{B} is the Biot coefficient, K_{SR} is the bulk modulus of the solid phase, $\beta_{T\text{F}}$ is the fluid compressibility under temperature, $\boldsymbol{\alpha}_{T\text{S}}$ is the thermal expansion tensor of the solid, $\dot{\mathbf{u}}$ is the solid matrix

velocity, Q_H is the fluid source/sink term, and div represents the divergence operator.

The mechanical balance equation, describing the conservation of linear momentum in the porous medium, is:

$$\operatorname{div}\left(\boldsymbol{\sigma}_{\mathrm{S}}^{\mathrm{E}} - \alpha_{\mathrm{B}} p \mathbf{I}\right) + \rho^{\mathrm{eff}} \mathbf{g} = \mathbf{0} \tag{5}$$

where $\boldsymbol{\sigma}_{\mathrm{S}}^{\mathrm{E}}$ is the effective stress tensor for the solid matrix, ρ^{eff} is the effective density of the porous medium, $\mathbf{g}$ is the gravitational acceleration, and $\mathbf{0}$ is the zero vector. The effective stress tensor is defined as:

$$\boldsymbol{\sigma}_{\mathrm{S}}^{\mathrm{E}} = \mathbf{C} : \left(\boldsymbol{\varepsilon} - \boldsymbol{\varepsilon}_{\mathrm{vp}} - \boldsymbol{\alpha}_{TS} \Delta T\right) \tag{6}$$

where $\mathbf{C}$ is the elastic stiffness tensor, $\boldsymbol{\varepsilon}$ is the total strain tensor, $\boldsymbol{\varepsilon}_{\mathrm{vp}}$ is the viscoplastic strain tensor, $\boldsymbol{\alpha}_{TS}$ is the thermal expansion tensor of the solid, and ΔT is the temperature change.

The effective properties of the porous medium are defined as:

$$(\rho C_p)^{\mathrm{eff}} = (1 - \phi_{\mathrm{F}}) \rho_{\mathrm{SR}} C_{p\mathrm{S}} + \phi_{\mathrm{F}} \rho_{\mathrm{FR}} C_{p\mathrm{F}} \tag{7}$$

$$\lambda^{\mathrm{eff}} = (1 - \phi_{\mathrm{F}}) \lambda_{\mathrm{SR}} + \phi_{\mathrm{F}} \lambda_{\mathrm{FR}} \tag{8}$$

$$\begin{aligned} \tilde{\mathbf{w}}_{\mathrm{FS}} &= \phi_{\mathrm{F}} \mathbf{w}_{\mathrm{FS}} = \phi_{\mathrm{F}} (\mathbf{v}_{\mathrm{F}} - \mathbf{v}_{\mathrm{S}}) \\ &= k_{\mathrm{rel}} \frac{\mathbf{k}_i}{\mu_{\mathrm{FR}}} (-\nabla p + \rho_{\mathrm{FR}} \mathbf{g}) \end{aligned} \tag{9}$$

where ρ_{SR}, $C_{p\mathrm{S}}$, and λ_{SR} are the density, heat capacity, and thermal conductivity of the solid phase, respectively, λ_{FR} is the thermal conductivity of the fluid, k_{rel} is the relative permeability, $\mathbf{k}_i$ is the intrinsic permeability of the porous medium, μ_{FR} is the dynamic viscosity of the fluid, and $\mathbf{v}_{\mathrm{F}}$ and $\mathbf{v}_{\mathrm{S}}$ are the velocities of the fluid and solid, respectively.

The balance equations presented above were derived from the hybrid method combining mixture theory and homogenization to address thermo-hydro-mechanical (THM) problems put forward by [36] and used in thermodynamically consistent continuum theories of porous media [6, 45]. These works form the basis for THM implementations in OpenGeoSys [25] and Code_Bright [30]. The approach proposed by [10], rooted in thermodynamic theory, has been implemented in the computational codes LAGAMINE [14] and Code_Aster [12]. [14] reviewed alternative methods for deriving balance equations, including mixture theory, where phases are treated as continuous media occupying the entire space, with properties determined by their interactions [6]. This approach is foundational for COMSOL Multiphysics [9], which employs a mixture theory framework for modeling multiphase coupled processes. Another method uses homogenization on local volumes, treating the system as interpenetrating continua, with phase-specific balance equations averaged to derive macroscopic equations [19–21]. This approach was foundational for Code_Bright [30]. In the past, these various theoretical approaches helped to form a coherent picture of porous media physics on the continuum and pore scale. Despite their emphasis on different aspects of the underlying theory, they lead to very similar model formulations in the present context.

The specific implementations of the codes used for this benchmark (see Table 6) were thoroughly discussed and compared in detail in the first benchmark study to this work by [40].

3.2 Main features of the analyzes

In accordance with the benchmark specifications, the modeling teams developed different numerical models. They consist of a two-dimensional plane strain domain, where only one cell is modeled, and the interaction between cells is provided by the symmetry conditions. The models assume a domain extending from 0 to 1000 m depth, which encompasses geological layers such as Kimmeridgian, Oxfordian, USC, UT, UA (subdivided into three sublayers UA1, UA2 and UA3), and Dogger. The parameters characterizing these formations are already presented in Tables 2, 3 and 4. As previously mentioned, all formations except the COx claystone are characterized by an isotropic elastic model, whereas a transversely isotropic elastic model is employed for the COx materials. One refers to [40] for a description of isotropic and transversely isotropic elasticity.

Due to symmetry, all models consider only half of the domain, extending to the midpoint between two cells, which also represents a line of symmetry. The model by BGE features 59700 quadrilateral elements with quadratic shape functions for the displacement, ensuring a detailed and accurate representation of the geological strata. A mesh of 13310 nodes and 12863 quadrilateral elements was adopted by UPC, with smaller elements near the gallery. The mesh developed by EDF for the far-field benchmark consists of a total of 27194 elements with a triangular mesh in the COx and a quadrangular mesh elsewhere. LEI discretized the domain into 2696 triangular and quadrangular quadratic mesh elements. The COx layer was meshed with triangular elements, whereas the other layers consist of quadrilateral elements. The model by ANDRA consists of 5228 elements. The mesh created by ULG uses quadrilateral elements (MWAT) with 8 nodes [8]. The total number of elements in this mesh is 4575. Figure 5 shows an example of mesh used for the present study developed by UPC.

The lithological profile for COx along with the initial temperature, pore water, and stress distribution along the Y-axis was implemented based on the provided field data

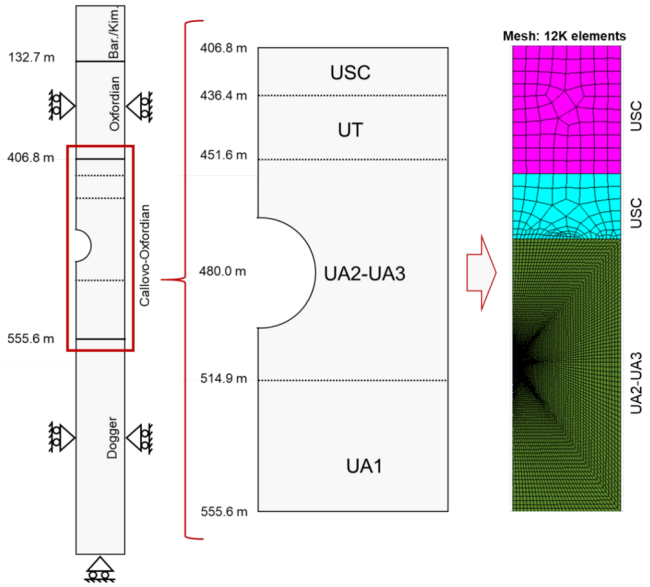

Fig. 5 Example of numerical model for the far-field case developed by UPC [11]

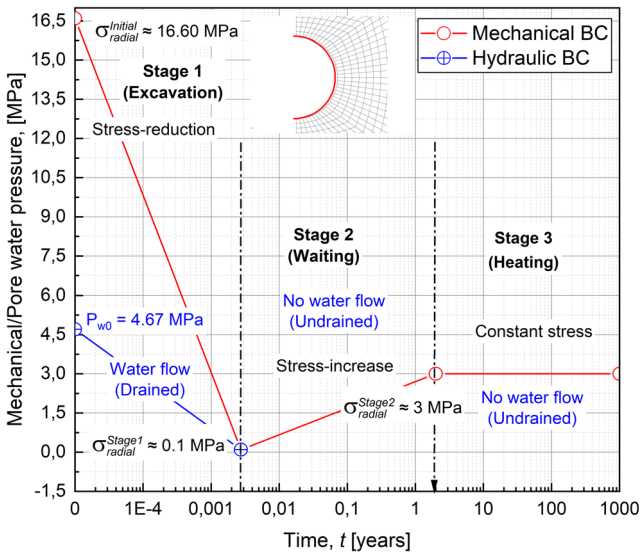

Fig. 6 Implementation of time varying boundary conditions at the borehole wall during excavation, waiting, and heating phase (modified after [11])

(see Fig. 2). The initial conditions consider the concept of effective stress from Biot. The majority of codes work with the total stresses so that the Biot effective stresses are processed in the codes directly. For OpenGeoSys, the effective stresses were specified as input and were first computed taking into account the Biot coefficient in each geological layer and the overpressure observed in the COx layer. In this context, a Python routine was developed to facilitate the initialization of stresses and pore pressure in the model.

Adiabatic and no-flow boundary conditions are assumed at the left, right, and bottom boundaries of the model, with normal displacements fixed. These conditions imply a conservative assessment of THM effects. In the cell, thermal, hydraulic, and mechanical loads are applied as functions of time. The stress at the tunnel boundary is completely deconfined within 24 h, followed by an isotropic pressure build-up to 3 MPa, simulating the swelling pressure of bentonite in the annulus between the liner and the surrounding rock. This pressure is maintained for up to 1000 a. The mechanical boundary conditions were mimicked using the stress reduction method as shown in Fig. 6 along with the flow conditions. The draining boundary condition was changed to a non-flow boundary condition for pore water pressure after the excavation phase. The heating phase was represented by the prescribed heat flux of two different thermal loads dependent on time (in W m^{-1}) over the tunnel boundary starting after the waiting phase.

4 Benchmark results

In the following, we present the simulation results of the proposed THM benchmark. Because the results of the two scenarios are similar, only one scenario is discussed in this section. In the next section, we will discuss a comparison of the effect of the different thermal loads applied resulting from scenarios 1 and 2.

The benchmark results will be discussed for three of the six specified points. The observation point P2 located at one diameter (that is, 1 m) from the wall of the gallery

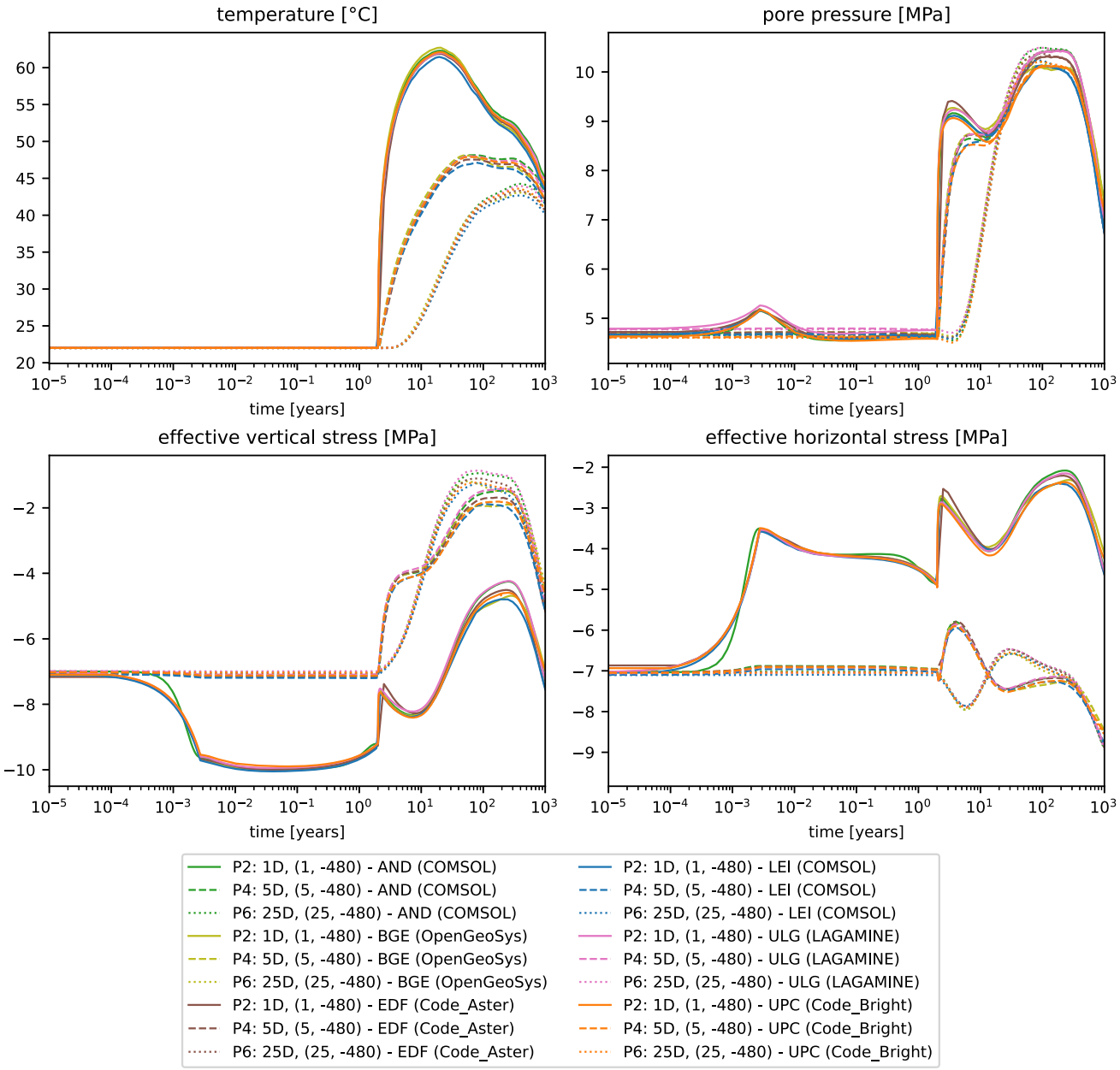

Fig. 7 Benchmark results for scenario 1 at observation points P2, P4, and P6

gives information about the kinetics of the THM process near the cell. The second point of interest is P4, which is located 5 diameters from the gallery and helps to understand the evolution of THM deeper in the rock where the rock is expected to be intact. The last point of analysis is P6 located in the middle of two adjacent cells. At this location, the superposition of the THM effects coming from the two cells is maximum.

The benchmark results are presented for scenario 1 in Fig. 7. The temperature evolution is shown on the top left. The evolution of the pore pressure is shown in the upper right. The evolution of effective stresses are presented in the bottom part of the figure with vertical stresses on the left and horizontal stresses on the right. The results for the observation points computed by different teams are depicted such that colors indicate the teams and line styles the points.

Temperature evolution: In the context of THM simulation in non-swelling clays under full saturation, the temperature evolution is not affected by the hydraulic and mechanical response of the rock. Thus, the temperature evolution is only a function of the assumed thermal parameters for specific geological layers [32]. Starting from the natural and undisturbed geothermal rock

temperature, a sharp increase in temperature is observed at all points. The temperature increase is delayed by the distance to the cell wall. Global temperature maxima of about 62, 48, and 44 °C are estimated for the points P2, P4, and P6. The exact timing of this peak varies among the different points, but all models show a peak within the range of 10 to 20 years, aligning with the results of [1, 5, 32]. These peaks are due to the thermal output assumed for Scenario 1, which acts as a localized heat source. This indicates that the maximum thermal influence is located near the wall of the gallery. In reverse, it can be stated that the impact of the waste's thermal output diminishes with distance from the cell. A second peak of minor amplitude (local maximum) can be observed at all curves in an advanced time around 275 years for the three observation points that results from the superposition of the thermal heat coming from the adjacent cells. This effect is specifically considered when assuming symmetric boundary conditions. After reaching the first peak, the temperature begins to decrease as the thermal output of the waste packages diminishes over time. At the end of the simulation, all temperature curves are converging toward a lower stable value of approximately 45 to 40°C after 1000 years.

The results are consistent among all the teams. The maximum temperatures and the rate of decline vary among the models, which may be attributed to differences in the mesh used by different teams, as the assumed thermal conductivity and heat capacity values of the rock in each simulation were given and the advection contributions are small. BGE results tend to be higher at all points, as LEI computed the lowest temperature. The range of results is in the range of less than 2 K. The general agreement between the peak temperatures in the simulations suggests that all models capture the essential physics of the heat conduction process in the saturated rock.

Pore pressure evolution: The results of the evolution of the porous pressure show an initial rise at P2 followed by a subsequent decline to the initial hydrostatic level around the first day of simulation. The increase in pore pressure is the result of "anisotropic deconfinement" occurring in the rock during excavation [26]. During excavation, horizontal stresses decrease and vertical stresses increase in the horizontal direction near the wall of the gallery, as can be observed in the corresponding graphs of effective vertical and horizontal stress on the left and right bottom of Fig. 7. This results in a volume reduction (compaction) at the sidewall, especially in anisotropic materials with higher stiffness in the horizontal bedding plane, as is the case for COx. In low-permeability media, where pore water is almost trapped in the pores, this compaction leads to an increase in pore pressure. This effect occurs near the cell wall because it cannot be observed deeper in the rock, for example, at P4. Although the findings related to the vertical direction are not included in this study, it is crucial to highlight that anisotropic deconfinement in the crown region results in expansion, which subsequently causes a reduction in pore pressure there. The subsequent decline is due to the applied stress increase at the borehole. This results in an increase in radial stresses that helps to mitigate the effect of anisotropic deconfinement.

In time, a sharp increase in pore pressure is observed at all points. The increase is delayed for points P4 and P6 located deeper in the rock. This pressure increase is the result of thermal pressurization, which correlates with the thermal field generated by the applied heat load. A first peak in pore pressure is observed in P2 and P4 near the gallery at two to three years, while the pore pressure still increases at P6. This indicates that the pore pressure builds up from the cell toward the domain limit, ultimately reaching the right-symmetry boundary of the model. The pore pressure decline following the peak clearly distinguishes the subsequent rise which is due to another mechanism.

In subsequent evolution, a second peak is observed at all points, which is even higher than the first one. This is due to the no-flow condition at the model boundary reflecting the effect of adjacent cells. The maximum pore pressure develops at P6 between two cells, indicating that this region is most affected by thermal pressurization due to superposition of pore pressure evolution coming from adjacent cells. The maximum pressure value observed at P6 is also almost reached at points P2 and P4, evidencing a convergence of pore pressure toward the same value and reflecting a homogenization of pore pressure at the repository level due to the superposition effect. With time and following the decrease in temperature, a decrease in the pore pressure is observed at all points after the second peak. The behavior of pore pressures at larger timescales, beyond the scope of the study, is not depicted on the graph. However, one can expect a long-term equilibration of pore pressures toward the initial conditions when the temperature increase eventually vanishes and excess pressures dissipate.

In general, the results obtained by all teams are satisfactory. The variability among the different models is naturally expected due to the discrepancies observed among the temperature results of the different teams. The agreement of the pore pressure peaks with the expected behavior from the study provides validation for the teams' ability to simulate the complex interactions of thermal and hydraulic processes within the geological formation.

Effective stress evolution: The effective stress components were evaluated following the Terzaghi effective stress framework. As already mentioned, the effective horizontal stress decreases and the vertical one increases near the gallery at P2 during excavation. In the waiting

phase, the applied swelling pressure affects in particular the vertical stress that recovers, whereas the horizontal stress remains almost unaffected at P2. In the meantime, there is no mechanical response deeper in the rock at P4 and P6 due to excavation and subsequent application of swelling pressure.

In the heating phase, the effective stress components follow the kinetics of the pore pressure evolution marked by a double peak owing to thermal pressurization near the cell and the superposition effect from the combination of THM effects of adjacent cells. The effective horizontal stress in the far field at P4 and P6 is not significantly affected by the thermal and hydraulic processes that occur in the near field of the cell due to the applied heat. The amplitude of stress change due to thermal and hydraulic loading is limited to 1 to 2 MPa. This slight variation over time, as seen in the effective horizontal stress graph, could be attributed to the volumetric expansion of the rock mass caused by the increase in temperature and pore pressure. However, according to [32], since this expansion is horizontally restricted, the increase in effective stress due to excess pressure of the pore water is minimal.

The effective vertical stress, as depicted in the effective vertical stress graph, gradually decreases from its initial quasi-isotropic condition. This decrease follows the rise in the temperature-induced pore pressure. Consistent stress reduction indicates a relaxation of vertical stress, which can be associated with thermal expansion and increased pore pressure, which reduces the effective stress. The observed relaxation of stress at all points, which is on the order of a few MPa, aligns with the findings of other studies such as those of [7, 32, 39]. Higher temperatures, and consequently higher pore pressures, would result in even lower values of vertical effective stress. As also pointed out by [32], if the effective vertical stress component decreases below the tensile strength of the rock, it could potentially lead to damage or the creation of fractures. This stress evolution is therefore critical for the design of the repository layout to avoid tensile failure. However, a stress recovery is observed when the temperature and pore pressure start to decrease near the end of the simulation. The full recovery can be expected as soon as the temperature increases and the excess pore water pressure vanishes.

The results obtained by all teams are generally consistent. At P2, a higher variability is observed for the two effective stress components. This was already discussed in the first part of this study in [40] and can be explained by the different meshes employed by the modeling teams coupled with higher gradients at the cell wall making the stress interpolation to the specified points cumbersome. This discrepancy vanishes deeper in the rock when the gradients decrease. The remaining discrepancies at P4 and P6 can be explained by the type of mesh (triangular or quadrilateral) and the interpolation functions (linear or quadratic) used by different teams. This was extensively discussed in [40].

5 Discussion

The results obtained show that the effective vertical stress decreases over time, and the effective horizontal stress remains relatively constant. Lower values of the effective vertical stress component could indicate areas where tensile failure is a risk. Interestingly, the rock region affected by this phenomenon is located deeper in the rock in the middle between adjacent cells but not near the cell where the temperature increase is maximum. As already mentioned, the higher the temperature, the more significant is this effect. In order to estimate the stress relaxation due to the higher thermal load, the comparison of results for the two thermal load scenarios is discussed in this section. In addition, the evaluation of the findings obtained in this benchmark will be verified in a subsequent analysis in which elastoplastic models are used for the formation of COx.

5.1 Comparison between scenario 1 and 2 (variation of the heat load)

The results obtained by all teams for the two scenarios considering an initial thermal load of $139\,\mathrm{W\,m^{-1}}$ and a higher initial thermal load of $242\,\mathrm{W\,m^{-1}}$ are evaluated in Fig. 8 for the observation point P6. The region surrounding this point has been identified in the previous section as the most at risk with regard to tensile damage induced by thermal fluid pressurization. In the figure, Scenarios 1 and 2 are denoted by heat loads 1 and 2, respectively.

At this point, the temperature is higher for heat load 2 as expected. The maximum temperature increases from 45°C to more than 50°C when the thermal load is increased. For this scenario, the first temperature peak resulting from the heat propagation resulting from the applied thermal load on the cell wall is higher than the second peak resulting from thermal superposition. This means that the energy input is too high to be dissipated in the rock as in scenario 1 under the same thermal properties, thus leading to a heat accumulation in the formation. Interestingly, the relatively small temperature difference of more than 5 K leads to an additional increase in the pore pressure of up to 4 MPa. This indicates that the induced effect of heat on the evolution of the pore pressure is overproportional. The resulting relaxation of the effective vertical stress is also equal to 4 MPa according to the concept of effective

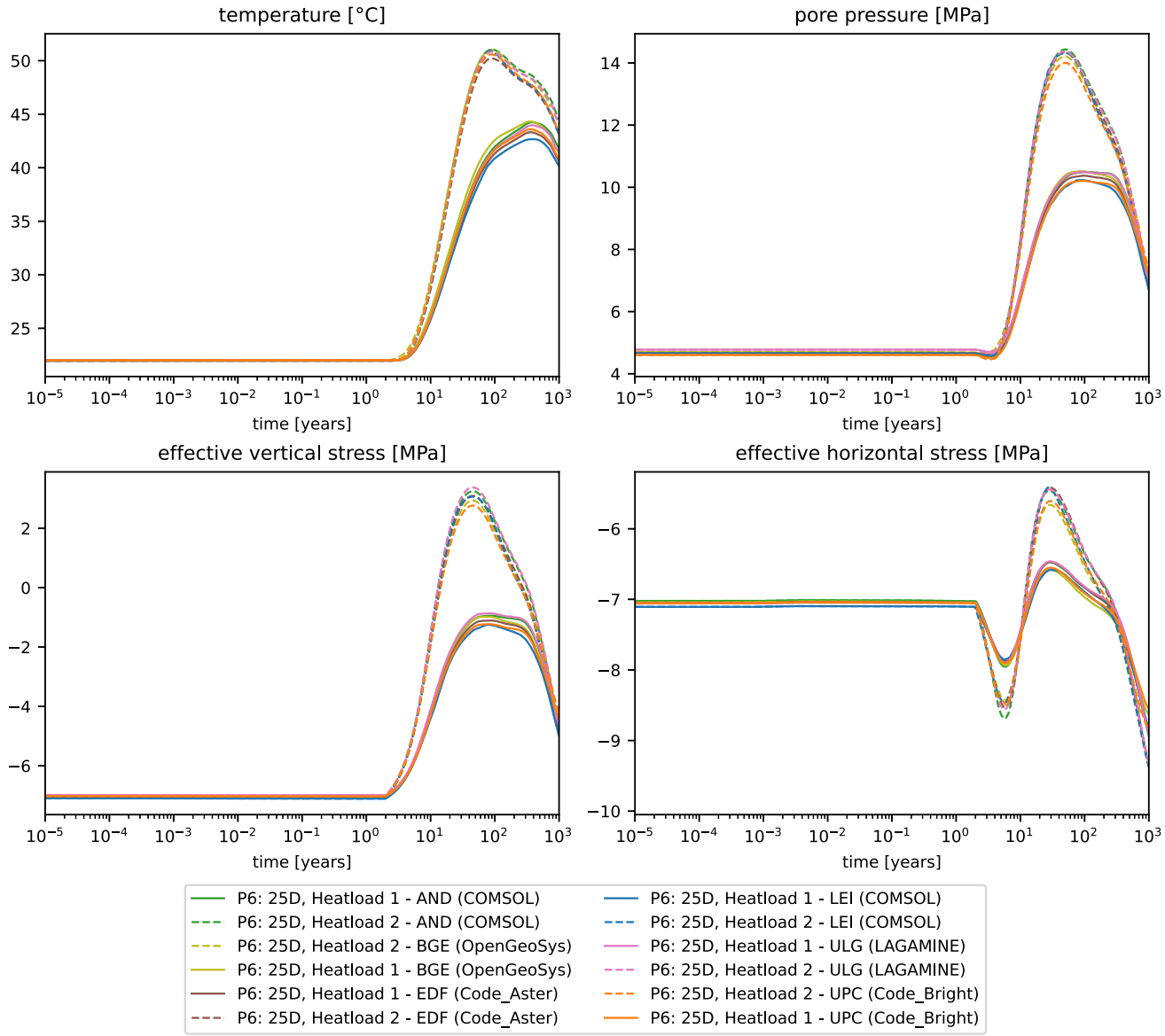

Fig. 8 Benchmark results for scenarios 1 and 2 at observation point P6

Terzaghi stress. In particular, effective tensile stress states have now been reached. The effective horizontal stress component increases in the meanwhile by 1 MPa and is therefore less affected by the effect of overpressurization in formation due to the deformation constraint and remains more affected by thermal strains.

In summary, the results for scenario 2 for all variables show that the rock mass experiences higher temperatures, leading to overproportionally higher pore pressures and substantial stress changes, which are crucial factors to consider in the design and safety assessment of the deep geological repository.

5.2 THM evolution of the repository system

The results presented so far give an insight into the evolution of THM in a horizontal direction at the disposal level. To understand the evolution of THM in the whole formation, we processed the temperature, pore pressure, and stress evolution along the depth of the formation. The results of this analysis are presented in Fig. 9. Each graph shows a series of isochrones, which are curves that represent the same time points in the evolution of the system. The time points 0, 2, 50, 100, 500, and 1000 years were selected for this evaluation.

The analysis is based on the initial prescribed conditions, where the pressure of the pore water is set to 0.1 MPa at the surface and 8.9 MPa at a depth of 1000 m.

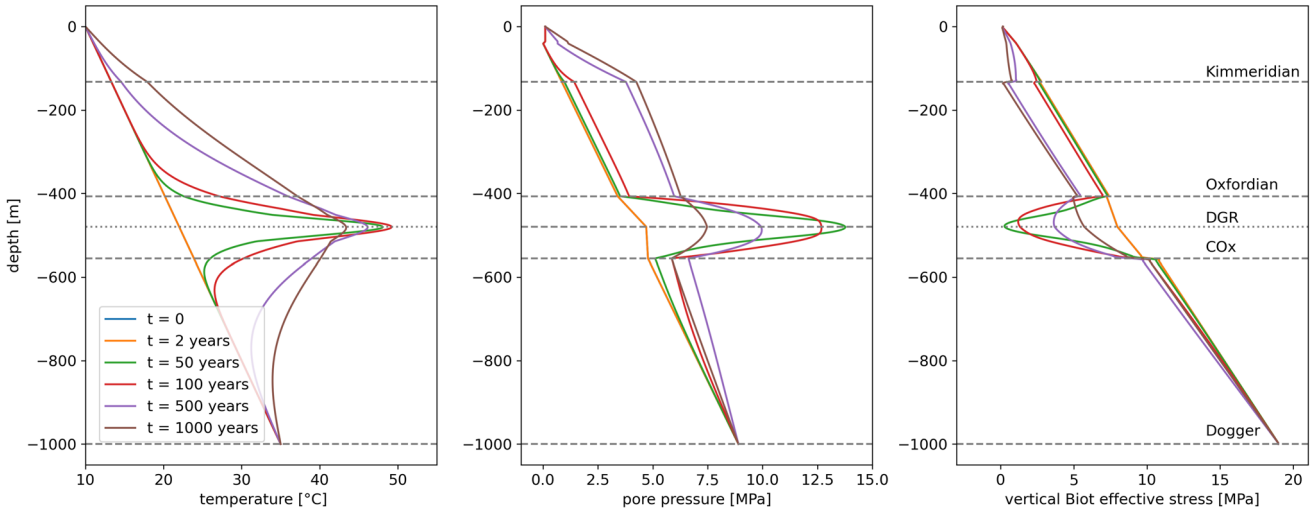

Fig. 9 Isochrones of temperature, pore pressure, and effective stress at 25 m (25D) along the depth for scenario 2 with initial thermal load of 242 W m^{-1}

The excess pore pressure induced by temperature is primarily concentrated within the COx layer, highlighting its sensitivity to thermal impacts. This response indicates that the COx layer undergoes significant pressure variations as a result of its low permeability and the thermal pressurization effect.

The Oxfordian layer, located above COx, exhibits more prominent variations in the pressure of the pore water caused by temperature due to its higher intrinsic permeability (10^{-16} m^2). This permeability allows for greater fluid movement and redistribution of pressure, contrasting with the behavior of the less permeable COx layer.

The Dogger layer, situated below the COx, also experiences thermal and hydraulic effects similar to those observed in the Oxfordian layer, albeit with reduced intensity due to a relatively smaller permeability compared to the Oxfordian layer. However, the fixed pressure boundary condition of 8.9 MPa at a depth of 1000 m influences the pore pressure results in this layer. Without this constraint, the pore pressure profiles in the Dogger would likely resemble those observed in the Oxfordian layer, reflecting a more uniform response to thermal and hydraulic loading.

The temperature profile shows a constant surface temperature of 10°C and a geothermal gradient that reaches 35°C at depth, as prescribed by the benchmark. During the heating phase, temperature changes are most pronounced in the COx layer and its adjacent layers (the Oxfordian above and the Dogger below). The significant temperature increases within the COx layer reflect the thermal loading from the repository, and adjacent layers are also affected to a lesser extent according to their distance to the heat sources and their respective permeability values.

The effective vertical Biot stress reflects the results of the evolution of the pore pressure in the formation. The stress profiles show a redistribution of stresses across the layers, with the most pronounced effects occurring in the COx layer. Stress relaxation is evident in this layer because of its low permeability and response to thermal pressurization. In the Dogger and Oxfordian layers, the stress redistribution is more gradual, reflecting their higher permeability and better hydraulic connectivity, which allows for more efficient stress dissipation.

This analysis underscores the critical role of the COx layer in the coupled thermal, hydraulic, and mechanical (THM) responses, driven by its low permeability and its central location within the geology in between two layers with higher permeability properties. The results also highlight that the maximum impact of THM on formation occurs during the early phase of repository evolution. As shown in the figure, the peak increase in pore pressure is observed at approximately 50 years, followed by a noticeable decreasing trend by 100 years, indicating the gradual dissipation of thermal and hydraulic effects over time.

5.3 Effect of plasticity on THM evolution

To investigate the mechanical damage to the COx formation caused by the thermal, hydraulic, and mechanical (THM) coupled evolution of the repository system, an additional analysis was performed using the model described in [27]. The model considers several behavioral features that are relevant for the satisfactory description of the COx behavior, such as strain hardening and softening, stiffness and strength anisotropy, rate dependence, and creep deformations. The model has been recently extended

Table 8 Parameters adopted for the constitutive model

Parameter	Value	Units
(Transversely isotropy)		
Young's modulus, $E_{\parallel}$	2500	MPa
Young's modulus, $E_{\perp}$	1250	MPa
Poisson's ratio, $\nu_{\parallel\parallel}$	0.25	-
Poisson's ratio, $\nu_{\perp\parallel}$	0.30	-
Shear modulus, $G_{\perp}$	628.2	MPa
Strength		
Initial friction angle, ϕ^*_{ini}	10	°
Peak friction angle, ϕ^*_{peak}	30	°
Residual friction angle, ϕ^*_{res}	16	°
Initial cohesion, $c^*_{0\,\mathrm{peak}}$	3	MPa
Initial tensile strength, $p_{\mathrm{t0\,peak}}$	1	MPa
Post-rupture ratio, r_{post}	0.01	–
Hardening parameter, χ	0.003	–
Hardening parameter, a_{hard}	0.001	–
Softening parameter, b_{post}	200	–
Softening parameter, b_{res}	2	–
Plastic potential		
Non-associativity constant, ω	0.05	–
Viscoplasticity		
Order of Perzyna's formulation, N	2	–
Viscosity parameter, η	10	day
Strength anisotropy		
Strength anisotropy parameter, Ω_{90}	1.3	–
Strength anisotropy parameter, Ω_{m}	0.819	–
Strength anisotropy parameter, δ_{m}	49.7	°
Strength anisotropy parameter, n	0.1	-
Creep		
Parameter in the creep law, γ	7.4e−7	MPa^{-1} day^{-1}
Parameter in the creep law, μ	0.3	–
Parameter in the creep law, m	50	–
Parameter in the creep law, ϵ_{thr}	5e-3	–
Temperature		
Reference temperature, T_{ref}	20	°C
Parameter for the evolution of strength with temperature, μ_{ϕ}	0.0	–
Parameter for the evolution of strength with temperature, μ_{coh}	0.35	–

to account for thermal effects, particularly the reduction of strength parameters with increased temperature. A detailed description of the model is out of the scope of this work and can be consulted elsewhere [26, 27]. The parameters used in this simulation are summarized in Table 8. They were derived through the THM simulation of a number of temperature-controlled triaxial tests in COx samples, as described in [11].

To better capture the effects of plasticity, a finer mesh consisting of 62000 linear quadrilateral elements was used in the analysis. The simulation was performed using OpenGeoSys for heat scenario 2 with shorter cooling time and higher thermal load of $242\,\mathrm{W\,m^{-1}}$. The initial and boundary conditions adopted for the elastic benchmark case were also applied in this analysis, as described in Table 1.

The primary objective of this study is to determine the extent to which plastic damage propagates over time within the COx formation as a result of THM impacts. Furthermore, the study aims to evaluate whether elastically-based THM integrity assessments of repositories in clay formations are sufficient to reliably demonstrate their long-term safety.

The results of this analysis are presented in Fig. 10. The figure presents the spatiotemporal evolution of plastic strain, pore pressure, and temperature over a 1000-year timescale. Snapshots are shown at specific time intervals ($t = 0$, 10, 20, 100, and 1000 years) to illustrate the progression of the THM processes.

The temperature field (top row) shows the thermal propagation of the disposal cell. At early times ($t = 10$ and $t = 20$ years), a steep temperature gradient develops near the heat source in an elliptical pattern as a result of the anisotropic thermal properties of the COx layer. Over time, heat dissipates radially outward, and by $t = 1000$ years, the thermal profile becomes more uniform, indicating the attenuation of thermal effects in the long term.

The pore pressure (middle row) contours illustrate the evolution of thermal pressurization effects over time, as well as their eventual dissipation. After excavation, the pressure distribution is influenced by the anisotropic deconfinement of the rock, resulting in a zone of high pore pressure in the horizontal direction near the gallery wall, while a zone of low pore pressure is observed in the vertical direction. By $t = 10$ and $t = 20$ years, a significant pore pressure build-up is observed. The high pore pressure propagates through the formation in an elliptical pattern, driven by the anisotropy in the thermal and hydraulic properties of the COx. By $t = 20$ years, this propagation results in pore pressures of at least 6 MPa across the entire disposal domain.

This homogenization of pore pressure was already observed in the elastic benchmark, as shown in Fig. 7 and Fig. 8, where the pore pressure at all observation points tended toward similar values over time. At later stages ($t = 100$ and $t = 1000$ years), the pressure gradients gradually dissipate, reflecting the long-term equilibration of hydraulic responses throughout the domain. However, at

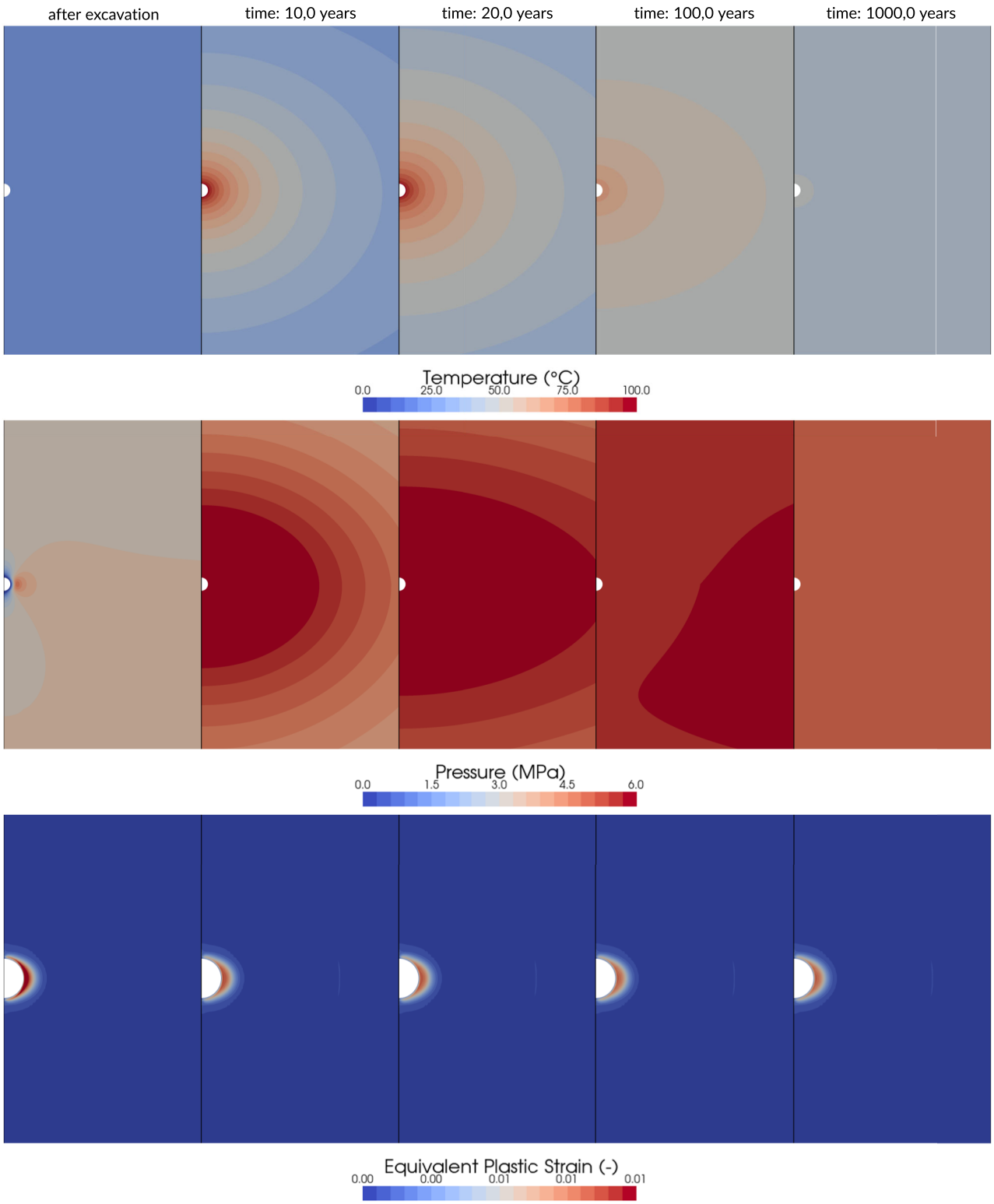

Fig. 10 Spatiotemporal evolution of temperature, pore pressure, and plastic strain in the COx formation over 1000 years following excavation and heating

$t = 100$ years, it is evident that the COx formation region experiencing elevated pore pressure continues to expand compared to $t = 20$ years, before dissipation begins to dominate.

The equivalent plastic strain snapshots (bottom row) indicate that there is no significant increase in plastic strain over time as a result of temperature effects. After excavation, the strain increment decreases slightly, while the extent of the plastic zone remains unchanged. This behavior is attributed to the elastoplastic model employed, which also incorporates viscoplasticity. Over time, the viscous effects diminish, leading to the observed reduction in strain increment. The extent of the plastic deformation highlights the zone of influence, where damage to the rock is expected to occur. This zone, commonly referred to as the excavation damaged zone (EDZ), remains largely unchanged after the excavation was completed.

Similar conclusions have been reported by [23], using a phase field modeling approach, and by [13], who applied a comparable constitutive model within the Code_Bright framework. Both studies found that the mechanical impact of thermal loading is spatially limited and does not significantly extend beyond the immediate vicinity of the excavation. These findings reinforce the conclusion that temperature increases have a minimal effect on the development and propagation of the EDZ, suggesting that thermal effects do not substantially contribute to additional mechanical damage in the long term.

In general, the results of this study indicate that, for the type of waste with similar decay heat assumed in this analysis and a maximum repository temperature of 100 °C, the extent of EDZ will not increase significantly due to THM impacts in the rock. The EDZ remains confined to the near field of the borehole, with its extent being less than one borehole diameter. These findings suggest that the integrity of deep geological repositories for temperature range below 100 °C can be effectively assessed using a thermo-poro-elastic approach, which is computationally several orders of magnitude more efficient. In addition, this approach allows for the integrity assessment of complex geological repository systems in three dimensions over extended periods of time.

6 Conclusions

The benchmarking exercise provided deep insight into the THM behavior of argillaceous formations as potential hosts for radioactive waste repositories. The collaborative effort of various European modeling teams offered a robust verification of the numerical tools used to simulate the THM processes that occur in clay-based repositories for radioactive waste. The results confirmed that argillaceous formations exhibit significant changes in temperature, pore pressure, and stress in response to the disposal of heat-generating radioactive waste. Temperature increases led to notable thermal pressurization effects, especially in the COx layer, indicating the potential for stress relaxation and changes in rock integrity over time. All models showed consistency in capturing the essential physics of heat conduction, pore water pressurization in low-permeability media, and the accompanying effective stress changes. A notable feature of the models was the use of inhomogeneous initial conditions, a mix of isotropic and anisotropic media, and intrinsically compressible solid phases ($b < 1$).

The use of an elasto-viscoplastic model in analyzing the THM response of the COx has shown that the Excavation Damaged Zone (EDZ) remained localized and stable, highlighting the limited effect of thermal loading on its evolution. Additionally, viscous effects contribute to the gradual relaxation of stress gradients and the dissipation of thermally induced overpressures. This finding supports the feasibility of repository designs that rely on the thermo-poro-elastic framework for assessing long-term safety, offering computationally efficient, yet, reliable solutions. In general, the study underscores the importance of validated and sophisticated modeling approaches in the design and evaluation of geological repositories safety, to ensure long-term containment and isolation of radioactive waste. The research sets a precedent for international collaboration in the promotion of nuclear waste management strategies, contributing valuable information to the global effort to ensure the safe and sustainable disposal of radioactive materials.

Acknowledgements The project leading to this work has received funding from the European Union's Horizon 2020 research and innovation program under grant agreement No. 847593. This work was supported by the German Federal Company for Radioactive Waste Disposal (BGE) as part of the project PIONIER [grant number: 45189414]. JB thanks BGE for funding the OpenWorkFlow project under research contract no. BGE STAFuE-21-05-Kle. TN acknowledges funding provided by the Federal Ministry for Education and Research (BMBF) under grant 03G0927B for the DigBen project and thank the Projektträger Jülich (PtJ) for support. The authors alone are responsible for the contents of this study. This paper describes objective technical results and analysis.

Funding Open Access funding enabled and organized by Projekt DEAL.

Declarations

Conflict of interest The authors declare no conflict of interest.

References

1. Andra (2005) Dossier Argile: evaluation of the feasibility of a geological repository in an argillaceous formation. Technical report, ANDRA. https://inis.iaea.org/records/pt1es-dqq15
2. Andra (2016) Dossier d'options de sûreté après fermeture (dos-af). Technical Report CG-TE-D-NTE-AMOA-SR2-0000-15-0062/A, Agence Nationale pour la Gestion des Déchets Radioactifs (Andra), Châtenay-Malabry, France. https://www.andra.fr/sites/default/files/2018-04/dossier-options-surete-apres-fermeture_0.pdf
3. Armand G, Noiret A, Zghondi J, Seyedi DM (2013) Short- and long-term behaviors of drifts in the Callovo-Oxfordian claystone at the Meuse/Haute-Marne underground research laboratory. J Rock Mech Geotech Eng 5(3):221–230. https://doi.org/10.1016/j.jrmge.2013.05.005
4. Armand G, Bumbieler F, Conil N, de la Vaissière R, Bosgiraud J-M, Vu M-N (2017) Main outcomes from in situ thermo-hydro-mechanical experiments programme to demonstrate feasibility of radioactive high-level waste disposal in the Callovo-Oxfordian claystone. J Rock Mech Geotech Eng 9(3):415–427
5. Bauer C, Plas F, Su K, Landais P (2004) La charge thermique d'un stockage—site de meuse / haute-marne. Technical Report C.NT.ASIT.03.118, Andra
6. Bowen RM (1980) Theory of mixtures, volume 1 of Applied mathematics and mechanics. Springer, New York
7. Christian B, Felix R, Gerik S, Thomas N, Olaf K, Jobst M (2019) Analysis of coupled thermo-hydro-mechanical simulations of a generic nuclear waste repository in clay rock using fiber surfaces. In: 2019 IEEE pacific visualization symposium (PacificVis), number 1, pp 189–201. IEEE. https://doi.org/10.1109/PacificVis.2019.00030. https://ieeexplore.ieee.org/document/8781565/
8. Collin F, Li X-L, Radu J-P, Charlier R (2002) Thermo-hydro-mechanical coupling in clay barriers. Eng Geol 64(2–3):179–193. https://doi.org/10.1016/S0013-7952(01)00124-7
9. COMSOL Multiphysics (2022) COMSOL Multiphysics Reference Manual. Version 6.0, COMSOL AB, Sweden
10. Coussy O (2004) Poromechanics. John Wiley & Sons, Chichester
11. de Lesquen C, Vu M, Simo E, Tatomir A, Vargas P, Bésuelle P, Dal Pont S, di Donna A, Zalamea N, Raude S, El tabbal G, Dizier A, Seetharam S, Narkuniene A, Collin F, Song H, Rawat A, Gens A, Song F (2023) Modelling report on the effect of temperature on clay host rocks behaviour. Technical Report EURAD-WP7-HITEC-Deliverable-7.6, Andra, BGE, CNRS-UGrenoble, EDF, EURIDICE, SCK CEN, LEI, ULiège, UPC. https://doi.org/10.13140/RG.2.2.28546.29127
12. Électricité de France EDF (2024) Code_Aster Documentation—Manual R7.01.10: Modelings THHM. General information and algorithms. https://code-aster.org/doc/v12/en/man_r/r7/r7.01.10.pdf. Accessed 2025-04-09
13. Fei S, Antonio G, Stefano C, Carlos P, Gilles A, Huaning W (2024) Analysis of thermally-induced fracture of Callovo-Oxfordian claystone: From lab tests to field scale. Geomech Energy Environ 39:100579. https://doi.org/10.1016/j.gete.2024.100579
14. Frédéric C (2002) Couplages thermo-hydro-mécaniques dans les sols et les roches saturés: Étude théorique et numérique. PhD thesis, Université de Liège, Liège, Belgium. https://orbi.uliege.be/bitstream/2268/87866/1/PhdCollin.pdf
15. Gens A (2013) On the hydromechanical behaviour of argillaceous hard soils-weak rocks. In: Anagnostopoulos A, Pachakis M, Tsatsanifos C (ed), Proceedings of the 15th European conference on soil mechanics and geotechnical engineering—geotechnics of hard soils—weak rocks, volume 4, pp. 71–118, Athens, IOS Press. https://doi.org/10.3233/978-1-61499-199-1-71
16. Gens A, Vaunat J, Garitte B, Wileveau Y (2007) 2007 In situ behaviour of a stiff layered clay subject to thermal loading: observations and interpretation. Stiff sedimentary clays: genesis and engineering behaviour—geotechnique symposium in print, vo. 57, no. 2, pp 207–228. https://doi.org/10.1680/ssc.41080.0011
17. Gilles A, Nathalie C, Jean T, Seyedi Darius M (2017) Fundamental aspects of the hydromechanical behaviour of Callovo-Oxfordian claystone: From experimental studies to model calibration and validation. Comput Geotech 85:277–286
18. Gilles A, Fréderic P, Jean T, Arnaud D, Ling LX, Severine L (2023) Contribution of HADES URL to the development of the Cigéo project, the French industrial centre for geological disposal of high-level and long-lived intermediate-level radioactive waste in a deep clay formation. Geol Soc Special Publ 536(1):237–256. https://doi.org/10.1144/SP536-2022-98
19. Hassanizadeh SM, Gray WG (1979) General conservation equations for multi-phase systems: 1. Averaging procedure. Adv Water Resources 2(3):131–144. https://doi.org/10.1016/0309-1708(79)90025-3
20. Hassanizadeh SM, Gray WG (1979) General conservation equations for multi-phase systems. 2: mass, momentum, energy, and entropy equations. Adv Water Resources 2(4):191–203
21. Hassanizadeh SM, Gray WG (1980) Thermodynamic basis of capillary pressure in porous media. Water Resources Res 16(5):833–843. https://doi.org/10.1029/93WR01495
22. Hudson JA, Stephansson O, Andersson J, Tsang CF, Jing L (2001) Coupled T-H-M issues relating to radioactive waste repository design and performance. Int J Rock Mech Mining Sci 38(1):143–161. https://doi.org/10.1016/S1365-1609(00)00070-8
23. Jian-Fu S, Zhan Yu, Zaobao L, Minh-Ngoc V, Gilles A (2024) Numerical analysis of thermo-hydromechanical process related to deep geological radioactive repository. Deep Resources Eng 1(1):100001. https://doi.org/10.1016/j.deepre.2024.100001
24. Kell GS (1975) Density, thermal expansivity, and compressibility of liquid water from 0. deg. to 150. deg. Correlations and tables for atmospheric pressure and saturation reviewed and expressed on 1968 temperature scale. J Chem Eng Data 20(1):97–105. https://doi.org/10.1021/je60064a005
25. Kolditz O, Bauer S, Bilke L, Böttcher N, Delfs JO, Fischer T, Görke UJ, Kalbacher T, Kosakowski G, McDermott CI (2012) OpenGeoSys: an open-source initiative for numerical simulation of thermo-hydro-mechanical/chemical (THM/C) processes in porous media. Environ Earth Sci 67(2):589–599. https://doi.org/10.1007/s12665-012-1546-x
26. Mánica M (2018) Analysis of underground excavations in argillaceous hard soils - weak rocks. PhD thesis, Technical University of Catalonia. http://hdl.handle.net/10803/663452
27. Mánica Miguel A, Antonio G, Jean V, Gilles A, Vu M (2022) Numerical simulation of underground excavations in an indurated clay using non-local regularisation. Part 1: formulation and base case. Géotechnique 72(12):1092–1112. https://doi.org/10.1680/jgeot.20.P.246
28. Mohajerani M, Delage P, Sulem J, Monfared M, Tang AM, Gatmiri B (2012) A laboratory investigation of thermally induced pore pressures in the Callovo-Oxfordian claystone. Int J Rock Mech Mining Sci 52:112–121. https://doi.org/10.1016/j.ijrmms.2012.02.012
29. Oberkampf William L, Trucano Timothy G, Hirsch C (2004) Verification, validation, and predictive capability in

computational engineering and physics. Appl Mech Rev 57(5):345–384. https://doi.org/10.1115/1.1767847
30. Olivella S, Gens A, Carrera J, Alonso EE (1996) Numerical formulation for a simulator (code_bright) for the coupled analysis of saline media. Eng Comput 13(7):87–112. https://doi.org/10.1108/02644409610151575
31. Paul B, Frédéric B, Jens B, Christophe B, Peter C, Sarah D, Masaaki F, Martin H, Mark J, Michel MJ, Carlos MJ, Andreas M, Takahiro O, Kristof S, Naokata S, Tim V, Klaus W (2017) Mont Terri rock laboratory, 20 years of research: introduction, site characteristics and overview of experiments. Swiss J Geosci 110(1):3–22. https://doi.org/10.1007/s00015-016-0236-1
32. Philipp B (2019) Thermo-hydro-mechanical behavior of the Callovo-Oxfordian claystone: effects of stress paths and temperature changes. PhD thesis, Université Paris-Est. https://tel.archives-ouvertes.fr/tel-02483143
33. Philippe L, Georges V, Jacques D, Patrick L, Maurice P (2013) Lithologie, hydrodynamisme et thermicité dans le système sédimentaire multicouche recoupé par les forages Andra de Montiers-sur-Saulx (Meuse). Bull Soc Geol France 184(6):519–543. https://doi.org/10.2113/gssgfbull.184.6.519
34. Pitz M, Kaiser S, Grunwald N, Kumar V, Buchwald J, Wang W, Naumov D, Chaudhry AA, Maßmann J, Thiedau J, Kolditz O, Nagel T (2023) Non-isothermal consolidation: a systematic evaluation of two implementations based on multiphase and Richards equations. Int J Rock Mech Mining Sci 170(2022):105534. https://doi.org/10.1016/j.ijrmms.2023.105534
35. Pla C, Vu MN, Armand G, Rutqvist J, Birkholzer J, Xu H, Guo R, Thatcher KE, Bond AE, Wang W, Nagel T, Shao H, Kolditz O (2020) A reliable numerical analysis for large-scale modelling of a high-level radioactive waste repository in the Callovo-Oxfordian claystone. Int J Rock Mech Mining Sci 140:104574. https://doi.org/10.1016/j.ijrmms.2020.104574
36. Roland L, Bernhard S (1998) The finite element method in the static and dynamic deformation and consolidation in porous media, vol. 34. Wiley
37. Rumble J (2019) CRC handbook of chemistry and physics (100th ed.). Boca Rotan, FL
38. Seyedi DM, Plúa C, Vitel M, Armand G, Rutqvist J, Birkholzer J, Xu H, Guo R, Thatcher KE, Bond AE, Wang W, Nagel T, Shao H, Kolditz O (2021) Upscaling THM modeling from small-scale to full-scale in-situ experiments in the Callovo-Oxfordian claystone. Int J Rock Mech Mining Sci 144:104582. https://doi.org/10.1016/j.ijrmms.2020.104582
39. Seyedi D, Vitel M, Vu M-N, Armand G (2018) Key parameters controlling thermo-hydro-mechanical pressurization in callovo-oxfordian claystone. In: International symposium on energy geotechnics SEG-2018. https://doi.org/10.13140/RG.2.2.27195.05926
40. Simo E, de Lesquen C, Leon R, Vu M, Raude S, El Tabbal G, Dizier A, Seetharam S, Narkuniene A, Collin F, Song H, Gens A, Song F, Tatomir A, Nagel T, Buchwald J (2025) THM-modelling benchmark initiative on the effects of temperature on the disposal of heat-generating radioactive waste in clay formations. Acta Geotech 20(4):1621–1642. https://doi.org/10.1007/s11440-024-02502-w
41. Thomas N, Jörg B, Feliks K, Michael P, Thomas H (2024) Hierarchical modelling in benchmarking, analysis and code development for coupled geo?processes. PAMM, pp 1–9, 10. https://doi.org/10.1002/pamm.202400025. https://onlinelibrary.wiley.com/doi/10.1002/pamm.202400025
42. Tourchi S, Mánica MA, Gens A, Vaunat J, Vu MN, Armand G (2024) A thermomechanical model for argillaceous hard soils-weak rocks: application to THM simulation of deep excavations in claystone. Géotechnique, (in press). https://doi.org/10.1680/jgeot.23.00023
43. Wenqing W, Hua S, Karsten R, Thomas F, Olaf K, Thomas N (2021) Analysis of coupled thermal-hydro-mechanical processes in Callovo-Oxfordian clay rock: from full-scale experiments to the repository scale. Eng Geol 293:106265. https://doi.org/10.1016/j.enggeo.2021.106265
44. Wileveau Y, Cornet FH, Desroches J, Blumling P (2007) Complete in situ stress determination in an argillite sedimentary formation. Phys Chem Earth 32(8–14):866–878. https://doi.org/10.1016/j.pce.2006.03.018
45. Wolfgang E (2002) Foundations of multiphasic and porous materials. Springer, Berlin. pp 3–86. https://doi.org/10.1007/978-3-662-04999-0_1

Authors and Affiliations

Eric Simo[1,2] · Christophe de Lesquen[3] · Minh-ngoc Vu[3] · Simon Raude[4] · Ginger El Tabbal[4] · Asta Narkuniene[5] · Povilas Poskas[5] · Frédéric Collin[6] · Rawat Abhishek[6] · Hangbiao Song[6] · Antonio Gens[7] · Fei Song[7,11] · Rocio Paola Leon-Vargas[2] · Alexandru-Bogdan Tatomir[8] · Miguel Mánica[9] · Thomas Nagel[1,10,12] · Jörg Buchwald[1,10]

✉ Eric Simo
eric.simo@bge.de

[1] Geotechnical Institute, TU Bergakademie Freiberg, Gustav-Zeuner-Straße 1, 09599 Freiberg, Germany

[2] BGE TECHNOLOGY GmbH, Eschenstrasse 55, D-31224 Peine, Germany

[3] ANDRA, 1/7 rue Jean Monnet, Châtenay-Malabry, France

[4] EDF R&D, 7 Bvd Gaspard Monge, 91120 Palaiseau, France

[5] Lithuanian Energy Institute, 3 Breslaujos str., 44403 Kaunas, Lithuania

[6] Urban and Environmental Engineering Research Unit, Université de Liège, Allée de la Découverte 9, 4000 Liège, Belgium

[7] Department of Civil and Environmental Engineering, Universitat Politecnica de Catalunya, Jordi Girona 1-3, 08034 Barcelona, Spain

[8] BGE mbH, Eschenstrasse 55, D-31224 Peine, Germany

[9] Institute of Engineering, National Autonomous University of Mexico, 04510 Coyoacán, Mexico

[10] Helmholtz Centre for Environmental Research-UFZ, Permoserstraße 15, 04318 Leipzig, Germany

[11] School of Aerospace Engineering and Applied Mechanics, Tongji University, Siping Road 1239, 200092 Shanghai, China

[12] Freiberg Center for Water Research (ZeWaF), TU Bergakademie Freiberg, Freiberg, Germany